CHARACTERIZATION OF SECONDARY FLOWS IN A HIGH BLOCKAGE RATIO INTERNAL COOLING CHANNEL

I. Mayo[1]- O. Cildir - T. Arts

von Karman Institute for Fluid Dynamics – 'Jacques Chauvin' laboratory
Chaussée de Waterloo 72, 1640 Rhode-Saint-Genèse, Belgium
E-mail: [1]ignacio.mayo.yague@vki.ac.be

ABSTRACT

The three dimensional flow field inside a scaled up model of an internal cooling channel is examined experimentally by means of Stereoscopic Particle Image Velocimetry (SPIV) at a Reynolds number of 40000. The channel presents a square cross section with a set of seven equidistant square ribs placed perpendicularly to the main flow direction on one of the walls. The pitch to height ratio between consecutive ribs is equal to 10, while the height of the ribs causes a blockage of 30% of the channel height. The mean values of the three velocity components are measured between the 5th and 6th rib, in planes perpendicular to the main flow direction. These results are compared with the already two-component velocity measurements available in literature, evaluating the magnitude of the main and secondary flows in the inter-rib region. Moreover, the present setup allows the extension of the already existing 2D data by introducing additional investigated planes and by measuring the complete Reynolds stresses tensor as well as the turbulent kinetic energy.

NOMENCLATURE

CFD	Computational Fluid Dynamics
D	Channel side length (also hydraulic diameter)
h	Rib height
PIV	Particle Image Velocimetry
p	Pitch between two ribs
p_{amb}	Ambient pressure
p_s	Average ambient pressure downstream of the contraction
q	Turbulent kinetic energy
Re	Reynolds number
SPIV	Stereoscopic Particle Image Velocimetry
TIT	Turbine Inlet Temperature
U	Stream-wise mean velocity
U^*	Stream-wise mean velocity at (X/h,Y/h,Z/h)=(2,1.53,0)
U_b	Bulk velocity
V	Vertical mean velocity (normal to the ribbed wall)
W	Span-wise mean velocity
u'	Turbulent stream-wise velocity
v'	Turbulent vertical velocity
w'	Turbulent span-wise velocity
X	Stream-wise direction
Y	Ribbed wall-normal direction
Z	Span-wise direction
α	Angle between the optical axis and the perpendicular direction to the measurement plane

OPEN ACCESS
Downloaded from www.euroturbo.eu

Copyright © by the Authors

ρ	Density
μ	Molecular viscosity

INTRODUCTION

A great effort has been made in the past decades to increase the Turbine Inlet Temperature (TIT) in gas turbines and hence to improve the cycle efficiency and the specific power. The introduction of different cooling techniques in turbine blades not only allowed TITs significatively higher than the melting temperature of the employed materials but also the possibility of extending the lifespans of the different hot components. The book by Han et al. (Han, et al., 2012) provides an extended literature review and a wide analysis of the different cooling techniques, as well as a summary of the experimental and numerical methods commonly applied. In particular, rib-turbulated convective cooling has been demonstrated to be an efficient method to transfer the heat from the outer face of the blade to the internal coolant fluid. A look at the internal cooling techniques developed through the years until the present days is reviewed in the recent paper by Ligrani (Ligrani, 2013). Today, new experimental techniques allow for more detailed and accurate quantification of the heat transfer problem in the internal cooling systems, while computational methods are under development to achieve more and more realistic simulations suited to the increasing performance of the existing hardware.

A basic model of an internal cooling channel with high blocklage ribs perpendicular to the main flow direction was experimentally investigated by Casarsa et al (Casarsa, et al., 2002), and Casarsa & Arts (Casarsa & Arts, 2005). The available experimental techniques empowered exhaustive wall heat transfer and velocity measurements by means of Liquid Crystal Thermography and planar, two-dimensional Particle Image Velocimetry (PIV). The flow was shown to be massively separated behind the ribs, with a mean recirculation bubble extending from the trailing edge of each rib to about 4 rib heights dowstream of it, a small second recirculation bubble in front of the rib, and a third bubble on the top of the rib. One of the most important features of the flow was its three-dimensional character, mainly due to the presence of two strong contra-rotating streamwise vortices induced by the ribs. This feature was obvious from the 2D PIV measurements in planes perpendicular to the main flow direction (Casarsa & Arts, 2005). Nevertheless, two-dimensional planar PIV measurements were challenging in that configuration because of the present perspective error and the significant particle displacement in the direction perpendicular to the masurement plane. In this case, the stream-wise velocity component was required to correct the displacement recorded by the cameras and to obtain the cross-flow. Since the stream-wise velocity was only available at three different spanwise locations, the displacement correction was a result from a triangulation and an interpolation of the available data (Casarsa, 2003). Given that this methology introduced an important interpolation error, the results needed to be validated by a more accurate procedure. The use of Stereocopic PIV (SPIV) was therefore considered.

Considering that SPIV is able to simultaneously measure the three components of the velocity field in the investigated plane, it is also possible to obtain the complete Reynolds stress tensor and the total turbulent kinetic energy. More details about the SPIV principles can be found in (Prasad, 2000) and (van Doorne & Westerweel, 2007). The work of van Doorne and Westerweel demonstrated that SPIV measurements in laminar and turbulent pipe flows were feasable in a plane perpendicular to the main flow direction. The importance of a rigorous calibration was then pointed out to quantify accurately the velocity field, the secondary flows and the turbulence distribution. Another example of velocity measurements by means of SPIV is the work of Barros and Christensen (Barros & Christensen, 2011), where the two-points correlation, Proper Orthogonal Decomposition and conditional averaging were employed to investigate a fully developed turbulent channel flow in a wide plane perpendicular to the main component of the velocity vector. Regarding the flow in cooling

channels, Armellini et al (Armellini, et al., 2011) carried out both PIV and SPIV experiments in a trailing edge cooling channel model under static and rotating conditions.

From the computational point of view, several methods have been shown to be suited to the analysis of internal cooling channels. Lately, Large Eddy Simulations (LES) have shown to provide reliable predictions of these flow and heat transfer phenomena. Lohász et al (Lohász, et al., 2006) carried out LES computations of a portion of a channel with the same geometry and flow conditions as the one investigated here, by the use of periodic boundary conditions, with a fair agreement with the data in (Casarsa & Arts, 2005). More recently, Fransen et al (Fransen, et al., 2012) investigated the same case, also with periodic boundary conditions, showing a good agreement in the mean velocity field, in the turbulent quantities and in the heat transfer distribution, practically over the full wall.

The main goal of the present work is to introduce a SPIV setup that is able to perform velocity measurements in magnified models of internal cooling channels, providing more information and a higher degree of reliability than with two-dimensional planar PIV, especially in the cases where the flow presents a highly three-dimensional character. The selected model is the same as considered by Casarsa and Arts (Casarsa & Arts, 2005), which has been widely investigated. However, the latter data were subjected to a triangulation and an interpolation in planes perpendicular to the main flow direction, leading to a potential error. The present work endeavors at validating the available results and extending them. Despite of the fact that the selected geometry does not fully duplicates the characteristics of modern internal cooling channels, it is still widely employed in CFD code verification. The present measurements are also intended to provide support to these validations.

EXPERIMENTAL SETUP

The overall configuration of the experimental facility, sketched in Figure 1, is based on the previous investigation of Casarsa and Arts (Casarsa & Arts, 2005). The mass flow is provided by the suction of air at ambient temperature and pressure by means of a centrifugal blower placed at the exit of the test section. At the inlet, a 1500 mm long contraction accelerates the flow from rest to the required speed, with an ingress section of 300×300 mm^2 and an exit one of 100×100 mm^2, giving access to the test section.

The channel has a total length of 3200 mm, a square cross section of 100 mm side (D), and it is equipped with 8 ribs placed on one of the walls at 90 degrees to the main flow direction with a pitch (p) of 300 mm. The rib cross section is a square of 30 mm height (h), and a span of 100 mm. Therefore, the rib blockage is 30%, and the rib pitch to height ratio is 10. A settling chamber is placed between the exit of the channel and the blower in order to damp any disturbance to the flow coming from the blower.

Four pressure taps are located at 220 mm downstream the end of the contraction and 665 mm upstream of the first rib to monitor the difference of the static pressure with respect to the ambient pressure, $p_{amb} - p_s$, with a water manometer whose resolution is 0.1 mm H_2O (0.981 Pa). The bulk velocity, $U_b$is calculated as

$$U_b = \sqrt{\frac{2(p_{amb} - p_s)}{\rho}} \qquad (1)$$

where ρ is the density of the air, calculated by using the ideal gas law and the ambient pressure and temperature. The air viscosity is obtained from the Sutherland's formula at the ambient temperature. In order to test at the same conditions as in (Casarsa & Arts, 2005), a Reynolds number,

$$Re = \frac{\rho U_b D}{\mu} \qquad (2)$$

of 40000 is needed, corresponding to a bulk velocity of about 6 m/s and a pressure difference of 24 Pa (depending on the ambient conditions).

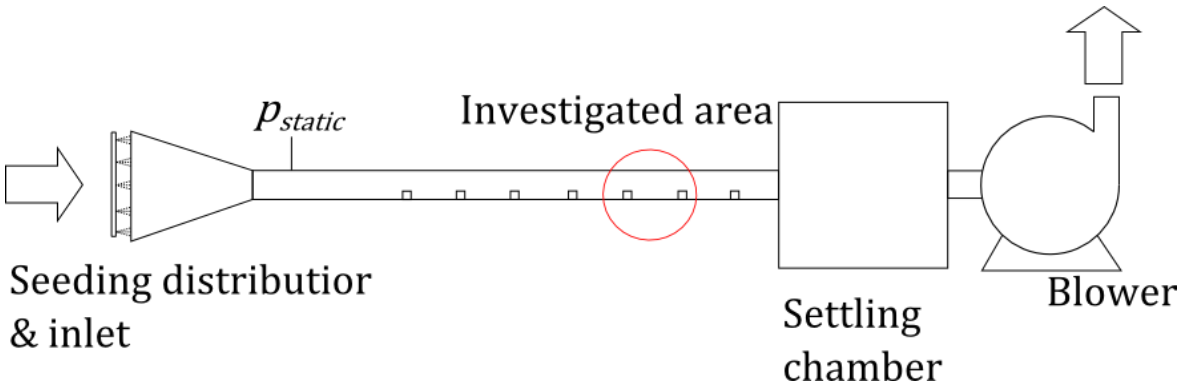

Figure 1. Sketch of the experimental facility, adapted from (Casarsa & Arts, 2005)

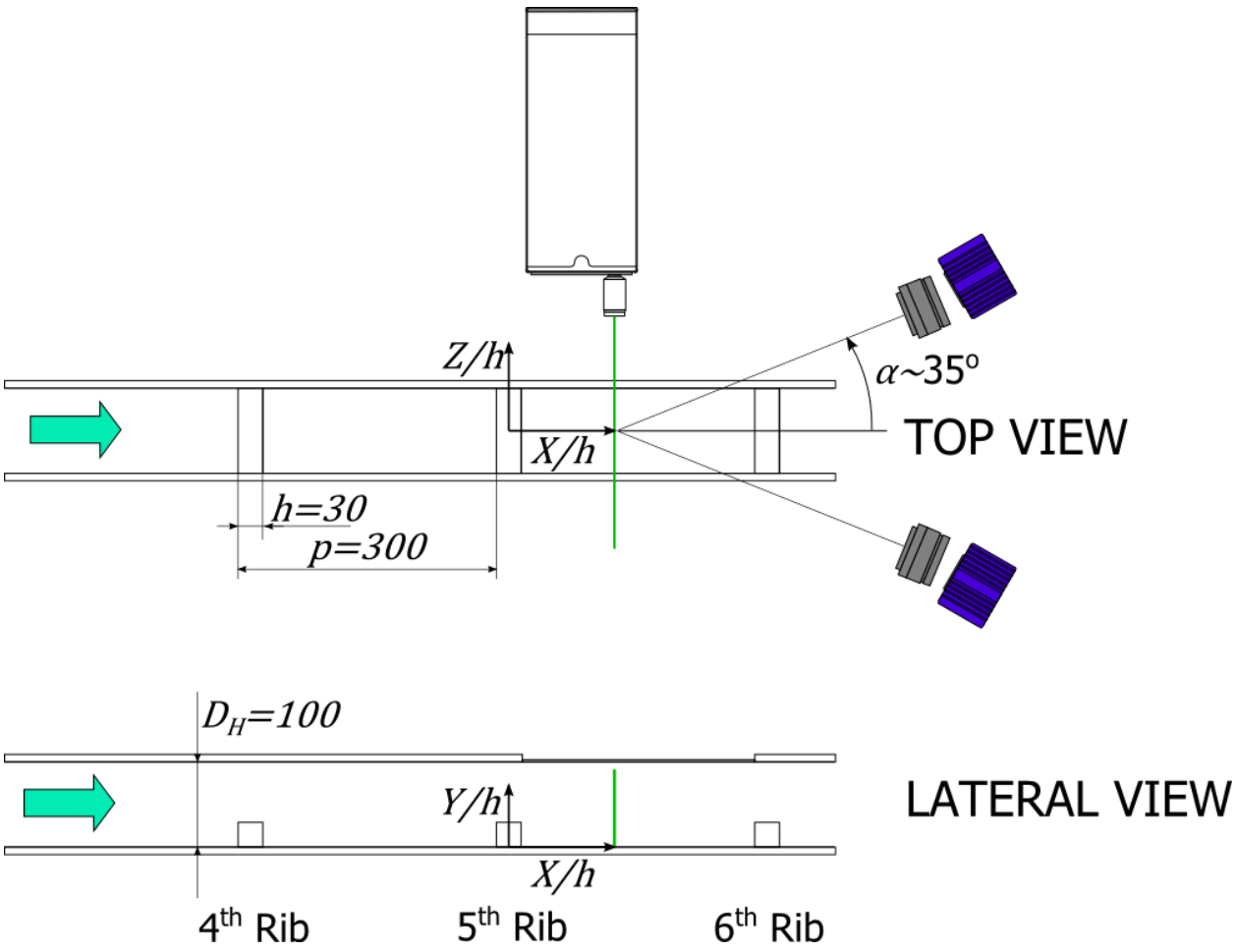

Figure 2. View of the Stereoscopic PIV system

The flow field is investigated in the area between the 5th and 6th rib by means of SPIV. Figure 2 shows a schematic view of the configuration of the experiment, with the origin of the frame of reference placed on the interface between the center of the 5th rib and the wall at mid-span. The X-direction is the main direction of the flow, whereas the XY plane is the symmetry plane of the channel. The studied planes are located at X/h=2, 4.33, 6.33 and 8.33, each of them with a surface of 100×90 mm^2, spanning from Z=-50 mm to +50mm with a maximum Y at 85 mm.

Two LaVision Imager SX 4M CCD dual-frame cameras are employed to acquire 1000 PIV images per plane with a resolution of 2360×1776 pixels, a pixel size of 5.5μm×5.5μm and a 12-bit grayscale depth. In order to record independent PIV realizations, the acquisition frequency is 5 Hz, corresponding to more than 8 times the characteristic turn-over time of the vortices with a size of the

order of the hydraulic diameter of the channel (D/U_b). The separation time between the frames of one realization is set at 25 μs in order to keep at least 75% of the particles within the laser sheet and therefore, maintain a good signal to noise ratio. Since the maximum velocity normal to the investigated plane is large (around 12 m/s) and the laser sheet thickness is about 1.5 mm, the particle normal displacement over the separation time is 5 times smaller than the laser sheet thickness.

The commercial software DaVis 8.1 (LaVision) is employed to obtain the three-dimensional flow field in the measurement planes. The software algorithm firstly dewarps the tilted view of the measurement plane from each camera, transforming it into a rectangle and calculates then the particle displacement. Therefore, the cross-correlation of the acquired images is performed in a common grid covering the measurement plane. More details about the processing algorithm are described in (Wieneke, 2005). The optical axis of each objective is placed at approximately 35º with respect to the normal direction to the measurement plane (LaVision GmbH, 2013), instead of the 45º often proposed (Prasad, 2000). Firstly, because a higher angle (45º) would more deform the image of the real interrogation area on the sensor of the camera, then the particle displacement observed by the camera decreases, and therefore the relative uncertainty increases. Secondly, the lower angle allows a larger overlapping of the investigated interrogation volumes, whose projections are slightly different on each of the camera sensors (Wieneke & Taylor, 2006). The interrogation volumes overlapping becomes crucial when high spatial gradients are present. The analysis of the PIV images is performed in two stages with interrogation windows of 64×64pixels^2 and 32×32 pixels^2, respectively, and with an overlapping of 50%. Two refinement steps are performed at each stage in order to offset the initial interrogation window and reduce the error due to the loss of correlation. The corresponding spatial resolution is about 2.5 mm (interrogation area size), whereas the vector spacing is 1.25mm.

The flow is seeded with corn oil particles of about 1 μm diameter generated by several Laskin nozzles. The particles are introduced upstream of the test section (Figure 1) by means of a seeding distributor. It consists in a frame to which the seeding generator is connected and distributes the seeding flow among evenly spaced drilled pipes allowing a uniform introduction of the particles at the inlet of the contraction. A Quantel EverGreen double-pulse Nd:YAG laser with a maximum energy of 200mJ/Pulse is used to illuminate the measurement plane. In the present case, only 40mJ/pulse are needed to obtain images of good quality.

Both cameras are equipped with a Nikon Nikkor objective (35 mm focal length). In order to achieve the Scheimpflug condition, the cameras are mounted on a support which allows the rotation of the camera with respect to the objective and consequently a fine focusing all over the studied plane. During the experiments, the objectives' f-number are set to values adapted to the intensity of the laser light and to obtain an image of the particle with a size of at least 3 pixels. The distance from the objective and the camera is set carefully in order to adapt the view of the investigated plane to the full height of the sensor of the camera. As a result, the approximate magnification factor in the Y-direction is 0.074 (13.5 pixel/mm) in the center with a maximum variation of ±0.004 at the top and bottom sides of the investigated plane, whereas the image magnification in the Z-direction is about 0.066 (12 pixel/mm) with a maximum variation of ±0.010 near the lateral walls.

A calibration plate with the same shape as the cross section of the channel, marked with a grid of circular dots of 1 mm spaced by 5 mm, is set in every measurement plane to build the mapping function that relates the image coordinate system (i.e. the sensor of the camera) with the real one. Moreover, the derivatives of this mapping function with respect to all the directions need to be determined. In order to establish all these components, the calibration plate is mounted on a micrometric system allowing its displacement in the X-direction with a resolution of 0.02 mm. The calibration plate is placed originally at approximately the center of the laser sheet and then it is displaced by 240 μm and 480 μm perpendicularly to the original plane. One picture is taken for each of the three locations to obtain the mapping function and its derivatives with respect to all the directions. The micrometric system is fixed to a flange incorporated on the top area of the channel to avoid any displacement with respect to the channel. Due to the thickness of the flange, no optical access is available in the upper 15 mm of the cross section of the channel, thus no data is acquired in

this region. After this, a self-calibration (included in the processing software) is employed to correct the mapping function due to the small misalignment between the calibration plate and the laser sheet (Wieneke, 2005).

RESULTS

The time-mean properties of the flow were calculated from the 1000 instantaneous realizations in each of the investigated planes. Figure 3 shows a descriptive view of the area between the 5th and 6th rib with the contours of the non-dimensional stream-wise mean velocity, U/U_b, over the investigated planes. Since the recirculation bubble extends up to approximately X/h=4.3 (Casarsa, et al., 2002), the plane at X/h=2 shows an important area covered by the recirculation bubble, whereas the plane at X/h=4.33 represents the flow field at the reattachment point. Due to the external flanges employed for the fixation of the calibration grid support, the area above Y/h=2.85 is not optically accessible and no data is available in this region. Moreover, due to proximity of the investigated planes at X/h=6.33 and 8.33, the 6th rib blocks the viewing of a portion of the flow field at those locations. In the case of the plane X/h=6.33, two small regions corresponding to the lower corners are covered by the rib, whereas the plane X/h=8.33 loses the information below Y/h=1.2 all along the span of the channel.

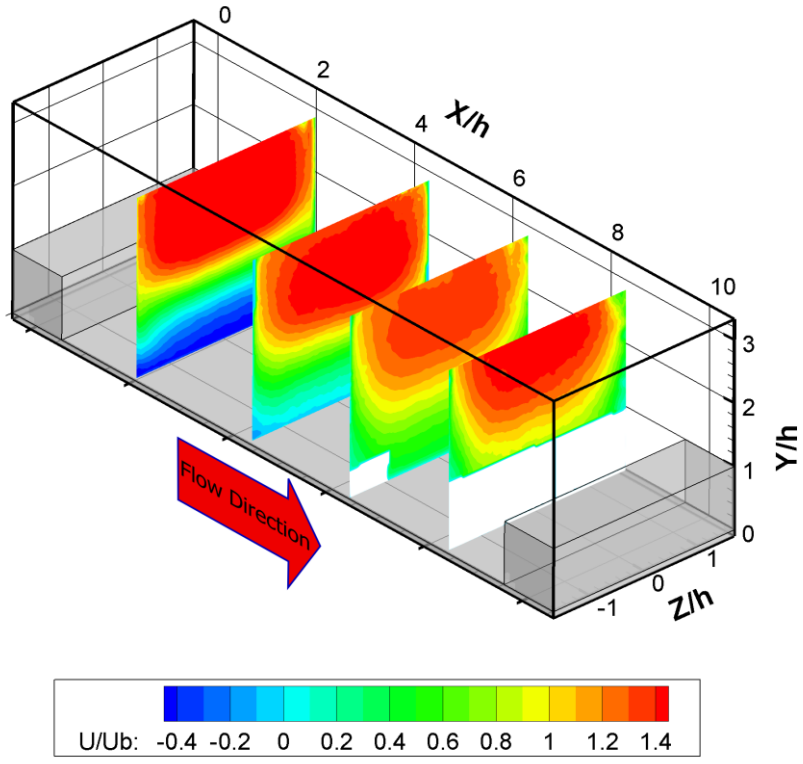

Figure 3. Stream-wise velocity contours in the investigated planes.

The stream-wise mean and turbulent velocities are extracted in the line $(X/h, Z/h)$=(2, 0) and compared in Figure 4 with the data presented in (Casarsa, 2003). Since the reference data was available only in dimensional form, the results are non-dimensionalized with the value of the stream-wise velocity at Y^*/h=1.53 (Casarsa, 2003), $U^* = U(2,1.53,0)$ In the present experiments, $U^* \approx 1.45U_b$. The time-mean stream-wise velocity presents a good agreement with the data of (Casarsa, 2003), with an overall difference of 2.5% of U^* and a maximum difference of 5.8% of U^* at Y/h=0.91. The agreement is fairly good in the case of the stream-wise velocity fluctuations, with an overall difference about 2.7% for U^* and a maximum difference of 6.4% of U^* in the closest interrogation area to the wall (Y/h≈0.05).

In order to confirm the validity of the results, additional comparisons with the two-dimensional PIV measurements (Casarsa & Arts, 2005) are made. Firstly, the streamlines generated from the velocity components normal to the main flow direction (V and W) in the planes X/h=2 and 4.33 are represented in Figure 5. The two rib-induced counter rotating vortices (Casarsa & Arts, 2005) are observed; their center is at Y/h=2.5 and Z/h=±1, with little or no variation in the position between planes X/h=2 and 4.33. The saddle point on the lateral walls (Z/h=±1.67) moves from Y/h≈1.5 at X/h=2 down to Y/h≈1 at X/h=4.33. As a consequence of the rib-induced vortices, two additional counter rotating vortices are present in the bottom area of the plane X/h=2 with their center at Z/h≈1, inside the recirculation bubble, inducing a circular motion in the opposite sense of the two original ones. The comparison with the streamlines reported in (Casarsa & Arts, 2005) and shown in Figure 5 (right) reveals the satisfactory agreement of the data, with an analogous layout of the streamlines, and a similar locations of the centers of the rib-induced secondary flows and of the saddle points on the lateral walls.

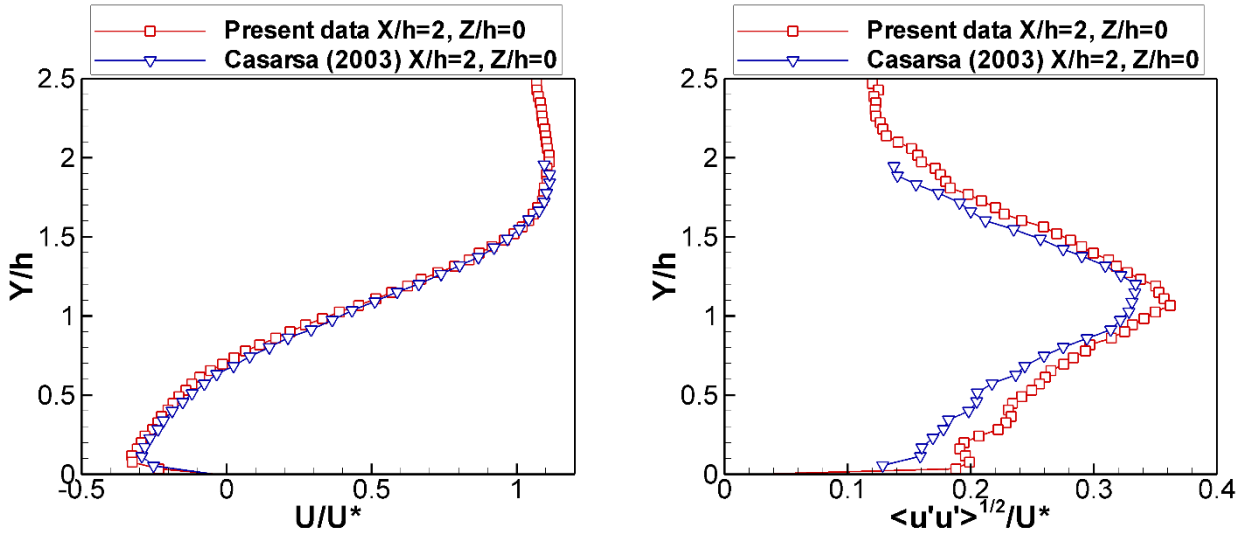

Figure 4. Comparison of the present data with (Casarsa, 2003) at (X/h, Z/h)=(2,0)

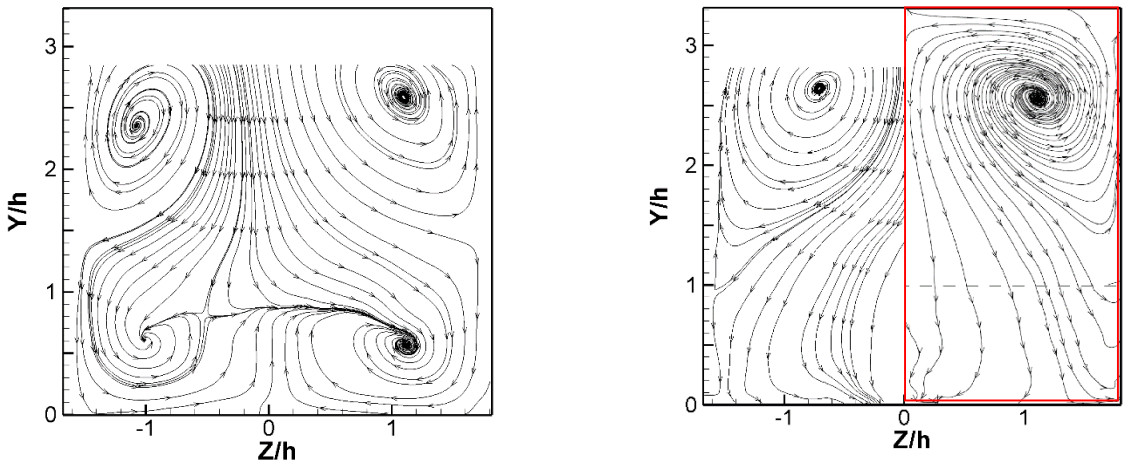

Figure 5. Secondary flows in the planes X/h=2 (left) and X/h=4.33 (right). The data from (Casarsa & Arts, 2005) is inside the marked rectangle.

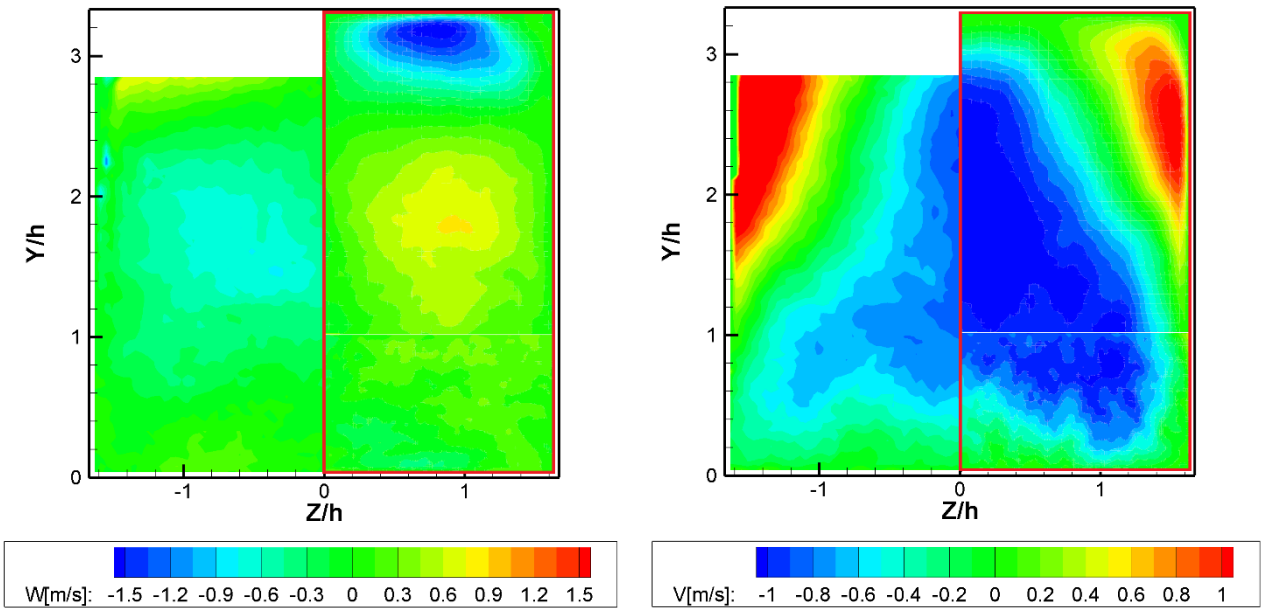

Figure 6. Comparison of the span-wise (left) and vertical (right) mean velocities with the 2D PIV data of (Casarsa, 2003) at X/h=4.33

The velocity components distributions normal to the main flow direction are compared with the PIV data of Casarsa (Casarsa, 2003) at X/h=4.33 in Figure 6. Due to the availability of the former data only in a dimensional form, the data could not be compared with the non-dimensional quantities. Therefore, some dissimilarities in the velocity magnitude were expected due to the different testing conditions (i.e. ambient pressure and temperature), even if the experiment would have been carried out in the same facility, with the same instrumentation and at the same Reynolds number. For instance, if the variations of the ambient temperature, pressure and Reynolds number are respectively of the order of 5ºC, 3000Pa and 2000, the impact on the bulk velocity is estimated as 0.4 m/s and on the vertical velocity of order of 0.1m/s. Nevertheless, the agreement is evident not only in the velocity distribution, but also in the magnitude. In the span-wise velocity contour, the fluid in the area between Y/h~1.5 to Y/h~2.5 tends to move towards the lateral walls with a maximum speed of about 0.71m/s (11% of the bulk velocity), because of the presence of the two rib-induced vortices. Due to the limitation in the optical access, the motion of the fluid towards the center of the channel in the area Y/h>2.85 is not visible in the present data. In the vertical velocity contour, the downwash motion can be observed in the lower part of the cross section due to the expansion of the fluid after the rib, with a maximum velocity of about 0.9 m/s (14% of U_b). Close to the upper corners, between the center of the rib-induced vortices and the lateral walls the flow is accelerated to speeds of about 1.9 m/s (30% of U_b) due to the proximity of the center of each vortex to the lateral wall.

Figure 7 shows the time-averaged non-dimensional stream-wise velocity contours at the four measurement locations. At X/h=2 there is an important velocity gradient in the Y direction due to the different momentum between the core of the flow and the recirculation bubble, and the distribution does not show a direct dependency with respect to the Z direction (only in the lateral boundary layers). As the fluid moves further downstream (X/h=4.33 and 6.33), the flow reattaches and the boundary layers develop. In this way, the stream-wise velocity field tends to be more uniform: the

high gradients in the Y direction due to the free shear layer originated by the rib are reduced, whereas the variations of the velocity in the Z direction are present at a wider distance from the lateral walls.

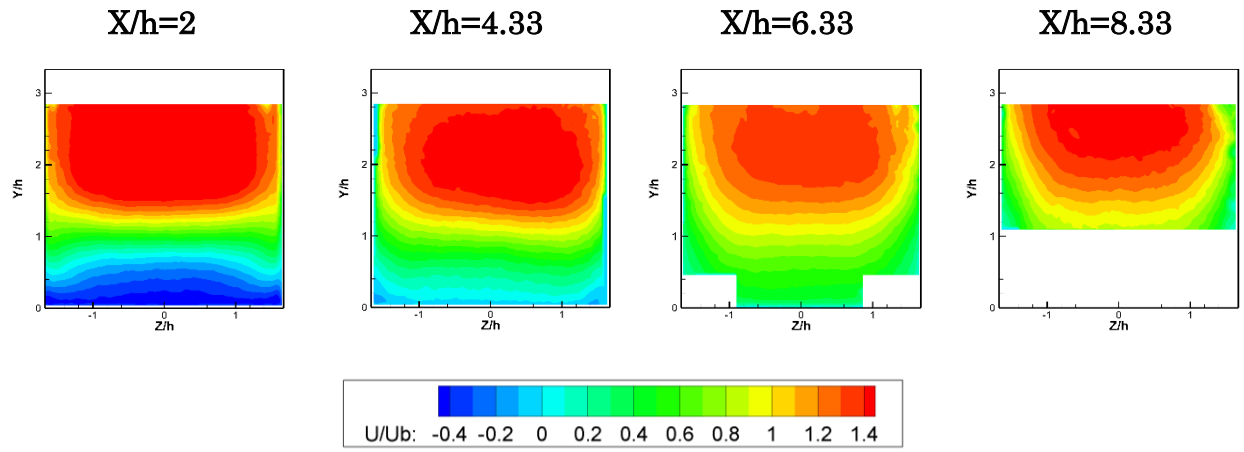

Figure 7. Stream-wise non-dimensional velocity component contours over the measurement planes

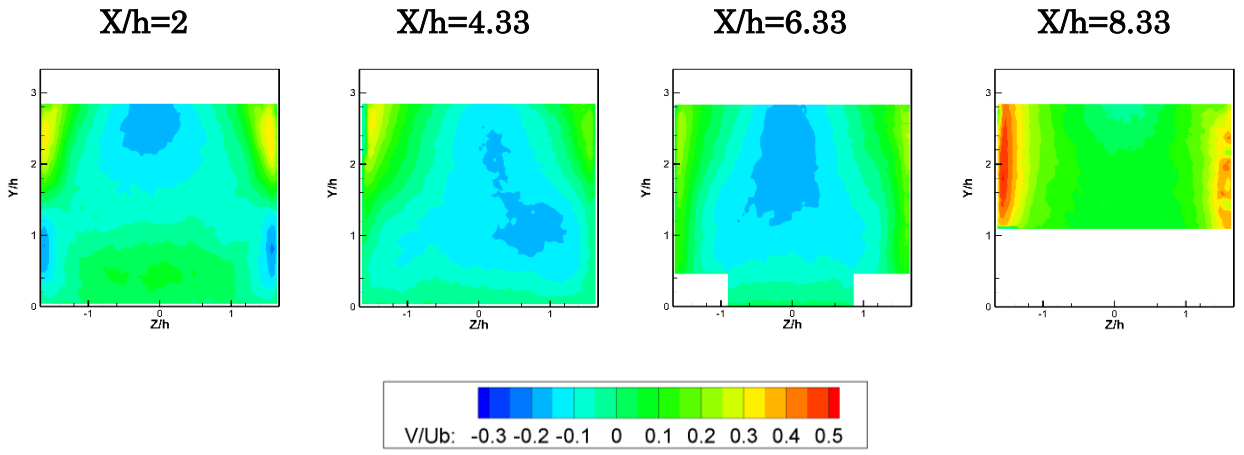

Figure 8. Vertical non-dimensional velocity component contours over the measurement planes

The evolution of the secondary flows is characterized in Figure 8. At X/h=2, the presence of the two upper rib-induced vortices forces a high positive vertical velocity in the lateral/top wall corner regions and a negative vertical velocity near the top wall in the vicinity of the symmetry plane. At the same time, the stream-wise vortices of the recirculation area generate a slightly positive velocity in the central region and a negative one close to the lateral walls. At X/h=4.33 the flow is reattached and there is no evidence of the recirculation bubble and, in turn, of the stream-wise vortices in it. The vertical velocity in this plane is mainly negative, with the exception of the lateral/top wall corner regions where the stream-wise vortices induce a positive vertical velocity. Downstream, the area of positive vertical velocity is extended to the almost complete area over the lateral walls. At X/h=6.33, the vertical velocity near the symmetry plane is negative, indicating that most of the fluid shows a swirling motion around the core of the stream-wise rib-induced vortices. At X/h=8.33, the proximity to the 6th rib is clearly felt since almost the whole flow field is subjected to a vertical velocity, especially close to the lateral walls.

Moreover, the non-dimensional vertical and span-wise turbulent velocities, $\sqrt{\overline{v'v'}}/U_b$ and $\sqrt{\overline{w'w'}}/U_b$ respectively, were calculated at X/h=4.33 in order to confirm the consistency of the

experimental setup by comparing the data by (Casarsa & Arts, 2005) and the present results. Figure 9 shows the good agreement of the SPIV data with the former 2D PIV measurements, with similar distributions and values. In the case of the vertical turbulent velocity, the maximum values (~40%) are found in the symmetry plane at a height Y/h~0.8, whereas the value in the core region is about 20%. On the other hand, the span-wise turbulent velocity shows analogous values with respect to the vertical turbulent velocity. The value of the vertical turbulent velocity rapidly decreases from the point of maximum turbulence to Y/h=0, likely limited by the proximity to the lower wall.On the other hand, the span-wise turbulent velocity remains high at smaller distances to the lower wall due to the moderate momentum and spatial gradients, and without constraints by the lower wall (Y/h=0). Close to the lateral walls, Z/h=±1.67, the constraint is now for the span-wise turbulent velocity. In this case, the gradient of the span-wise turbulent velocity in the Z-direction is more acute than that of the vertical turbulent velocity. The latter keeps a higher level in the region immediately close to the lateral walls.

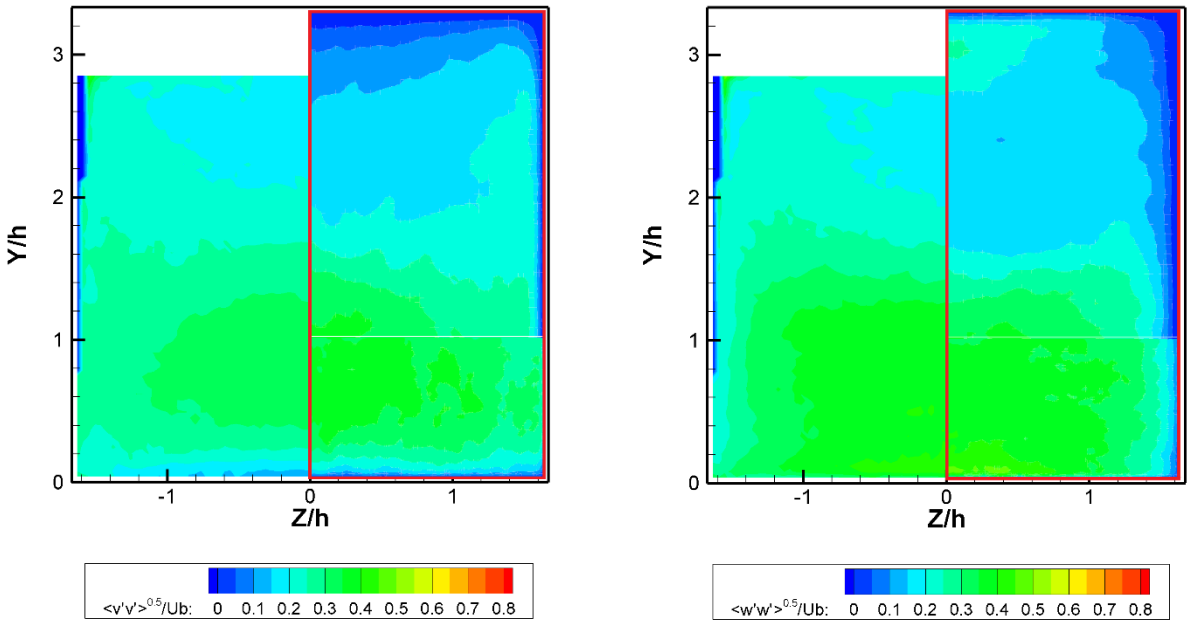

Figure 9. Comparison of the vertical (left) and span-wise (right) non-dimensional turbulence intensities with the 2D PIV data of (Casarsa & Arts, 2005) at X/h=4.33

Considering that the SPIV provides the three components of the velocity vector, the non-dimensional turbulent kinetic energy

$$q = \frac{\overline{u'u'} + \overline{v'v'} + \overline{w'w'}}{U_b^2} \qquad (3)$$

was obtained at X/h=2 and X/h= 4.33, and is represented in Figure 10. At $X/h = 2$, the maximum value of q is found in the free shear layer separating the core of the flow and the recirculation region (Y/h~1), with a value about 0.5. At the level Y/h~1, the value drops from the maximum to zero as the distance to the lateral wall is decreased. The minimum value of q is found in the core of the flow (Y/h~2.5, Z/h~0, q~0.08) and increases towards the lateral walls. Downstream, at X/h=4.33, the maximum value has slightly dropped to 0.46, but a wider area presents a q>0.4. In this plane, the core fluid shows a minimum q of 0.09.

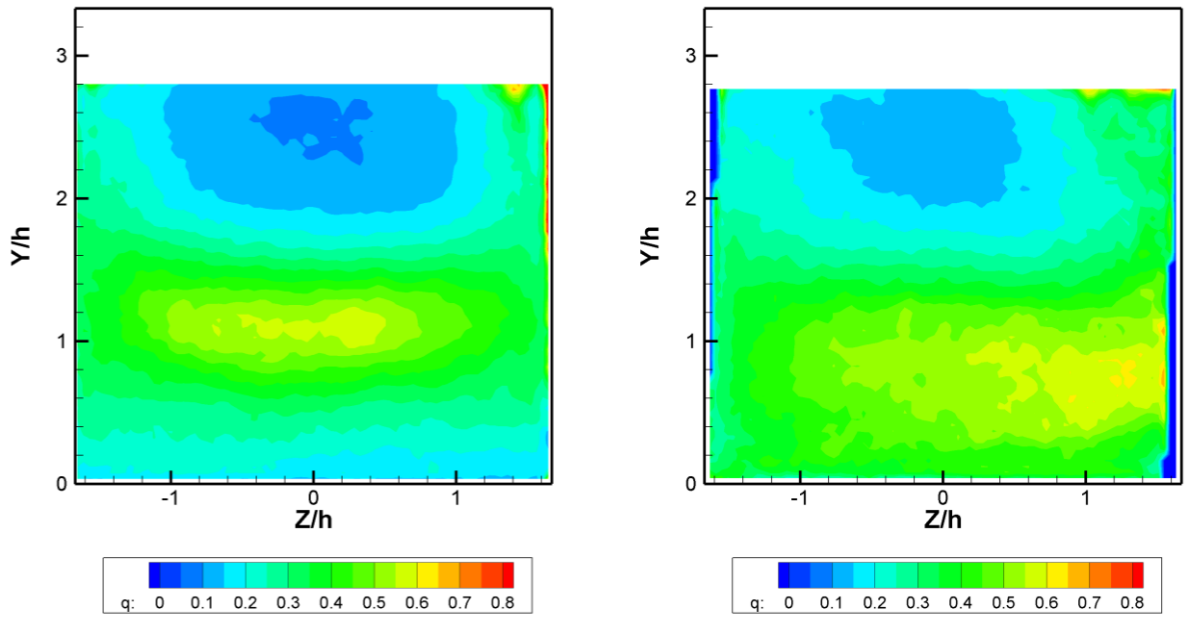

Figure 10. Non-dimensional turbulent kinetic energy at X/h=2 and X/h=4.33

CONCLUSIONS

Stereo PIV measurement were performed in a simplified model of an internal cooling channel and compared to the 2 × 2D results by Casarsa and Arts (Casarsa & Arts, 2005). The latter data represents a test case used in CFD code validations, but the measurements in planes perpendicular to the main flow direction were possibly affected by the error caused by the triangulation and interpolation of the stream-wise velocity profile obtained in three different span-wise locations and needed for a parallax correction. Moreover, although Stereo PIV has been widely used in Fluid Sciences, the application of this technique to the investigation of the flow field in the internal cooling channels of turbine blades is not yet widely spread. The capabilities of the experimental technique allow a further extension of the characterization of the flow field by providing the three components of the velocity field, the complete Reynolds stresses tensor, the total turbulent kinetic energy, etc.

The mean stream-wise velocity and turbulent stream-wise velocity show a good agreement with the previous data. The overall discrepancy in the stream-wise mean velocity and turbulent velocity are about 2.5% and 2.7% of U^*. A second comparison with the work of (Casarsa & Arts, 2005) was made in a plane perpendicular to the main flow direction and placed close to the reattachment area of the recirculation bubble, behind the 5th rib of the investigated channel. Results showed a good agreement in the distributions and values of the mean velocity field and normal Reynolds stresses. Additional measurements were performed in successive planes (X/h=2, 4.33, 6.33 and 8.33) to delve into the evolution of the stream-wise velocity, the secondary flows and the turbulent kinetic energy. At X/h=2, four stream-wise vortices were identified. The two upper ones were already observed a X/h=4.3 by Casarsa and Arts as a result of the presence of the rib. On the other hand, the two lower vortices were located in the recirculation bubble area just behind the rib. It is shown that the stream-wise velocity evolves to a distribution with decreasing gradients after the rib. However, the vertical velocity changes continuously due to the influence of the secondary flows and the streamline curvature caused by the ribs.

REFERENCES

Armellini, A., Casarsa, L. & Mucignat, C., 2011. Flow field analysis inside a gas turbine trailing edge cooling channel under static and rotating conditions. *Int. J. Heat Fluid Flow,* Volumen 32, pp. 1147-1159.

Barros, J. M. & Christensen, K. T., 2011. Cross-Flow Stereo PIV Measurements in Wall Turbulence. *7th International Symposium on Turbulent Shear Flow Phenomena.*

Casarsa, L., 2003. *Aerodynamic Performance Investigation of a Fixed Rib-Roughened Internal Cooling Passages,* s.l.: phD thesis, von Karman Institute & Universita degli Studi di Udine.

Casarsa, L. & Arts, T., 2005. Experimental Investigation of the Aerothermal Performance of a High Blockage Rib-Roughened Cooling Channel. *J. Turbomach.,* 123(3).

Casarsa, L., Cakan, M. & Arts, T., 2002. Characterization of the Velocity and Heat Transfer Fields in an Internal Cooling Channel with High Blockage Ratio. *Proceedings of ASME TURBOEXPO 2002,* Issue GT2002-30207.

Fransen, R., Gourdain, N. & Giquel, L. Y., 2012. Steady and Unsteady Modeling for Heat Transfer Predictions of High Pressure Turbine Blade Internal Cooling. *Proceedings of ASME Turbo Expo 2012,* pp. Paper GT2012-69482.

Han, J.-C., Dutta, S. & Ekkad, S. V., 2012. *Gas Turbine Heat Transfer and Cooling technology.* 2 ed. s.l.:Taylor & Francis.

LaVision GmbH, 2013. *FlowMaster Product Manual,* Göttingen, Germany: LaVision GmbH.

Ligrani, P., 2013. Heat Transfer Augmentation Technologies for Internal Cooling of Turbine Components of Gas Turbine Engines. *International Journal of Rotating Machinery,* Volumen 2013.

Lohász, M. M., Rambaud, P. & Benocci, C., 2006. Flow Features in a Fully Developed Ribbed Duct Flow as a Result of MILES. *Flow Turbulence Combust,* Volumen 77, pp. 59-76.

Prasad, A. K., 2000. Stereoscopic particle image velocimetry. *Exp. Fluids,* Volumen 29, pp. 103-116.

van Doorne, C. W. H. & Westerweel, J., 2007. Measurement of laminar, transitional and turbulent pipe flow using stereoscopic-PIV. *Exp. Fluids,* Volumen 42, pp. 259-279.

Wieneke, B., 2005. Stereo-PIV using self-calibration on particle images. *Exp. Fluids,* Volumen 39, pp. 267-280.

Wieneke, B. & Taylor, S., 2006. *Fat-sheet PIV with Computation of Full 3D-Strain Tensor using Tomographic Raconstruction.* s.l., 13th Int Symp on Applications of Laser Techniques to Fluid Dynamics, Lisbon, Portugal.